Available online at www.sciencedirect.com

ScienceDirect

journal homepage: www.elsevier.com/locate/watres

Stochastic collision and aggregation analysis of kaolinite in water through experiments and the spheropolygon theory

*Fiona H.M. Tang**, *Fernando Alonso-Marroquin*, *Federico Maggi*

Laboratory for Environmental Engineering, School of Civil Engineering, The University of Sydney, Bld. J05, 2006 Sydney, NSW, Australia

ARTICLE INFO

Article history:
Received 21 September 2013
Received in revised form
8 December 2013
Accepted 10 January 2014
Available online 23 January 2014

Keywords:
Suspended particle
Shape
Collision
Aggregation
Surface morphology
Stochastic analysis

ABSTRACT

An approach based on spheropolygons (*i.e.*, the Minkowski sum of a polygon with N vertices and a disk with spheroradius r) is presented to describe the shape of kaolinite aggregates in water and to investigate interparticle collision dynamics. Spheropolygons generated against images of kaolinite aggregates achieved an error between 0.5% and 20% as compared to at least 32% of equivalent spheres. These spheropolygons were used to investigate the probability of collision ($Pr[C]$) and aggregation ($Pr[A]$) under the action of gravitational, viscous, contact (visco-elastic), electrostatic and van der Waals forces. In ortho-axial (*i.e.*, frontal) collision, $Pr[A]$ of equivalent spheres was always 1, however, stochastic analysis of collision among spheropolygons showed that $Pr[A]$ decreased asymptotically with N increasing, and decreased further in peri-axial (*i.e.*, tangential) collision. Trajectory analysis showed that not all collisions occurring within the attraction zone of the double layer resulted in aggregation, neither all those occurring outside it led to relative departure. Rather, the relative motion on surface asperities affected the intensity of contact and attractive forces to an extent to substantially control a collision outcome in either instances. Spheropolygons revealed therefore how external shape can influence particle aggregation, and suggested that this is equally important to contact and double layer forces in determining the probability of particle aggregation.

1. Introduction

Suspended particle matter (SPM) is one of the primary contributors to biological, chemical and physical processes in natural aqueous environments (e.g., van Leussen, 1999; Lartiges et al., 2001; Cloern, 2001). In fact, SPM promotes microbial activities (e.g., respiration and growth, Riebesell, 1991; Boetius et al., 2000; Simon et al., 2002; Kiorboe, 2003; Maggi, 2009), biogeochemical nutrient cycling (e.g., Knowles, 1982; Herbert, 1999; Laverman et al., 2006), redox and remineralization processes (e.g., Anderson, 1982; Fowler and Knauer, 1986), and transport of organic and inorganic chemicals (e.g., nutrients, contaminants, hydrocarbon pollutants, *etc.*, Ongley et al., 1981; Lick and Rapaka, 1996; Tye et al., 1996; Leppard et al., 1998).

Numerical modelling of SPM has become an important approach to understand and predict SPM pathway and fate as

* *Corresponding author*. Tel.: +61 2 9351 2145.
E-mail addresses: fiona.tang@sydney.edu.au (F.H.M. Tang), fernando.alonso@sydney.edu.au (F. Alonso-Marroquin), federico.maggi@sydney.edu.au (F. Maggi).
0043-1354/$ – see front matter © 2014 Elsevier Ltd. All rights reserved.
http://dx.doi.org/10.1016/j.watres.2014.01.026

Abbreviations

δ	[L] Relative displacement
Δx_n	[L] Overlapping length
Δx_t	[L] Tangential elastic displacement
γ	[$ML^{-1}T^{-1}$] Fluid dynamic viscosity
κ	[L^{-1}] Reciprocal Debye length
λ	[T^{-1}] Coefficient of damping
ϕ	[$ML^2T^{-3}I^{-1}$] Surface electric potential
ε_0	[$T^4I^2M^{-1}L^{-3}$] Permittivity of vacuum
ε_r	[–] Dielectric constant of water
d	[L] Distance between spheropolyflocs surface
d_0	[L] Distance with neutral double layer force
d_c	[L] Distance between centers of mass of spheropolyflocs
g	[LT^{-2}] Gravitational acceleration
k	[MT^{-2}] Coefficient of stiffness
m	[ML^{-1}] Mass of spheropolyfloc per unit depth
r	[L] Spheroradius
r_{eq}	[L] Equivalent radius
v	[LT^{-1}] Velocity
$_n$	[–] Subscript of normal component
$_t$	[–] Subscript of tangential component
$\vec{F}_A$	[MLT^{-2}] Van der Waals attractive force
$\vec{F}_C$	[MLT^{-2}] Contact force
$\vec{F}_D$	[MLT^{-2}] Drag force
$\vec{F}_E$	[MLT^{-2}] Elastic force
$\vec{F}_G$	[MLT^{-2}] Gravitational force
$\vec{F}_R$	[MLT^{-2}] Electrostatic repulsive force
$\vec{F}_V$	[MLT^{-2}] Viscous force
H_A	[ML^2T^{-2}] Hamaker constant
I	[–] Reference pixel image
I_{SP}	[–] Spheropolygon image
M	[ML^{-1}] Effective mass of spheropolyflocs
N	[–] Number of vertices
$Pr[A]$	[–] Probability of aggregation
$Pr[C]$	[–] Probability of collision
RE	[%] Relative error
V	[–] Error between I and I_{SP} in pixels
FFT	Fast Fourier Transform
PBM	Particle-based model
SPM	Suspended particle matter

well as the transport of adsorbed chemicals and attached mircoorganisms. The majority of SPM transport models involve advective and sedimentary flows, which generally require the assumptions of spherical and non-porous particles as in the Stokes regime (Stokes, 1851). These assumptions provide analytical simplicity to describe particle–particle interactions (Wacholder and Sather, 1974), settling (e.g., Rubey, 1933; Clift et al., 1978; Krishnappan, 1990; Han and Lawler, 1991), collision rate (e.g., Abrahamson, 1975; Valioulis and List, 1984), and aggregation and breakup probability (e.g., Saffman and Turner, 1956; Han and Lawler, 1991). SPM transport models were improved when porous spherical particles were adopted (e.g., Kusters et al., 1997; Wu and Lee, 2001). Among many, Stolzenbach (1993) observed very distinct collision kinetics between porous and non-porous particles, and was able to achieve a better estimation of collision and aggregation probability using porous spheres. SPM models were further improved by fractal scaling laws, that is, higher-order aggregates were assumed to be made by (statistically) self-similar assemblies of lower-order aggregates (e.g., Krone, 1962; Meakin, 1991; Kranenburg, 1994; Maggi, 2007). Since then, fractal scaling laws, which often assumed aggregates to be made of multiple spherical primary particles, have been successfully used to describe settling velocity (e.g., Winterwerp, 1999; Vahedi and Gorczyca, 2011; Maggi, 2013), flocculation rate (e.g., Li and Logan, 1997; Serra and Casamitjana, 1998; Serra and Logan, 1999; Kim and Stolzenbach, 2004) and sediment fluxes (e.g., Kranenburg, 1994; Stone and Krishnappan, 2003).

In nature, however, neither SPM aggregates nor primary particles are perfectly smooth, solid spheres, but rather, they are irregularly-shaped bodies with varying shape, size and porosity. Parametric studies have addressed the significance of SPM shape as one of the factors that affects its dynamics (e.g., Clift et al., 1978; Dietrich, 1982; Vainshtein et al., 2004). For example, Corey shape factor (Corey, 1949), dynamic shape factor (Briggs et al., 1962), and Janke shape factor (Janke, 1966) expressed particle shape using complex empirical equations. These morphological studies, however, based on parametric quantities that may have limited effectiveness to describe particle shape and contact dynamics in an explicit way. Hence, we recognize the existing gaps in the characterization of SPM shape, the need to understand the extent to which SPM shape affects its dynamics, and how shape can explicitly be accounted for in experimental, theoretical and numerical investigations.

Here, we propose a morphological approach to describe the shape of SPM aggregates by using spheropolygons and we address the significance of accurate shape description on collision dynamics between suspended particles and aggregates using both experimental data and analytical tools. In this study, images of kaolinite aggregates suspended in water were acquired with a μPIV system, and were used to generate spheropolygons with different levels of accuracy. We then used these spheropolygons within a particle-based model (PBM) to assess various particle–particle interaction features such as (i) the probability of aggregation in relation to spheropolygon accuracy; (ii) effect of particle relative axial displacement on aggregation kinetics; and (iii) particle interactions within the double layer barrier. Analysis of these results led to the discussion of morphological effects on SPM collision and aggregation kinetics.

2. Methods

2.1. Experiments with kaolinite mineral

Kaolinite mineral (type Q38, with primary particle size (diameter) ranging between 0.6 μm to 38 μm) was hydrated in distilled water at a concentration of 8.8 g/L. A 20 ml suspension was poured into a 50 ml beaker and a magnetic stirrer was used to provide constant gentle mixing. SPM aggregates were sampled approximately 10 mm below the surface using a Pasteur pipette with 3 mm opening tip to reduce shear as

recommended in Gibbs and Konwar (1982), and were gently transferred to a Perspex tank. During both sampling and transferring, the pipette tip was fully submerged in the solution and aggregates were gently released. These procedures could reduce suction and shear resulting from pipetting that may lead to floc breakup.

Images of kaolinite aggregates settling down the Perspex tank were acquired using a μPIV system, which consisted of a CCD camera (Prosilica GC-2450), a high magnification lens (Navitar 12× Body Tube) and a Cree LED light source of 3.7 W. The CCD camera had a size of 2448 × 2050 pixel, 8-bit grayscale depth with a frame rate of 15 Hz at full size and was connected to a host computer. Aggregate images were then acquired using *Image Acquisition Toolbox* in Matlab R2012a. The magnification lens was equipped with a continuous zoom with magnification steps ranging from 0.58 to 7.0, which corresponded to a resolution from 4.4 × 4.4 μm^2 per pixel to 0.37 × 0.37 μm^2 per pixel. In this experiment, a magnification level of 2.5 was used, *i.e.*, the resolution was about 1 μm^2 per pixel.

Grayscale images of kaolinite aggregates, with intensity ranging from 0 (black) to 255 (white), were processed to separate the background from the region of interest. Fast Fourier Transform (FFT) was applied to remove high frequency background noise, whereas a two-threshold algorithm (*imadjust* function in Matlab R2012a) was used to adjust image intensity. Images were then converted to black and white with zeros for background (black) and ones for illuminated aggregates (white) based on threshold values calculated using *graythresh* function in Matlab R2012a. Images that contained out-of-focus aggregates were disregarded.

2.2. Definition of spheropolygon

A spheropolygon is defined as the Minkowski sum of a polygon with N vertices and a disk with radius r (also known as spheroradius) (Dobrohotoff et al., 2012)

$$P \oplus Q = \{u + v | u \in P, v \in Q\}, \tag{1}$$

where u and v are the sets of points belonging to the polygon P and disk Q, respectively. Note that $\oplus$ is symmetric (*i.e.*, $P \oplus Q \equiv Q \oplus P$). An example of spheropolygon with $N = 16$ and $r = 4$ μm is shown in Fig. 1.

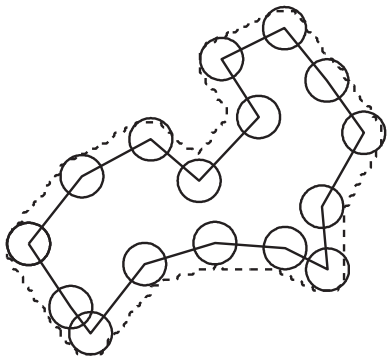

Fig. 1 – Polygon P with $N = 16$ (solid line) and disk Q with $r = 4$ μm (circles) are shown with the spheropolygon $P \oplus Q$ drawn (dashed line).

2.3. Spheropolygon optimization

The shape of kaolinite aggregates was approximated at various degrees of accuracy by using spheropolygons with different values of N and r. Processed images of kaolinite aggregates were used as the reference pixel image I to generate a spheropolygon image I_{SP}. The error V in pixels was determined as $V = P(|I_{SP} - I|)$, where $P(X)$ is a function that calculates the number of white pixels (*i.e.*, the number of *ones*) in the image matrix X.

Spheropolygon optimization consisted in minimising V by using an algorithm similar to that proposed in Dobrohotoff et al. (2012). To this end, each vertex with coordinates (x_k, y_k) with $k = 1,\ldots, N$ was incrementally moved in the plus and minus x and y directions from $-h$ to $+h$, with h the spatial discretization length. The error V resulting from each movement was updated and used to determine its gradient $\nabla V = (\delta V/\delta x, \delta V/\delta y)$, where $\delta V/\delta x$ and $\delta V/\delta y$ are the central differences. The vertex position in the next iteration was calculated by solving the equation of motion of that vertex (Allen and Tildesley, 1993),

$$H\nabla V + c\frac{\delta x}{\delta t} = \frac{\delta^2 x}{\delta t^2},$$

where $H = 0.5$ is the force factor and $c = 2$ is the damping factor. Iterations continued until the minimum V and the optimal spheropolygon (here called spheropolyfloc) was found. Spheropolyfloc accuracy was expressed by the percent error relative to I

$$RE = \frac{V}{P(I)} \times 100. \tag{2}$$

In this work, 17 values of N (ranging between 4 and 64), and 3 different values r (*i.e.*, $r = 1$ μm, 2 μm and 4 μm) were used to generate spheropolyflocs.

2.4. Spheropolyfloc interaction forces

Kinetic interactions between spheropolyflocs were modelled using a modified particle-based model (PBM) in a two-dimensional domain based on Alonso-Marroquin (2008). In this model, each spheropolyfloc undergoes gravitational $\vec{F}_G$ and drag $\vec{F}_D$ forces, which modulus is defined respectively as (Stokes, 1851)

$$F_G = mg, \tag{3}$$

$$F_D = 6\pi r_{eq} \gamma v, \tag{4}$$

where $m = \rho_s A$ is the spheropolyfloc mass per unit depth with ρ_s the surface density of kaolinite aggregates and A the spheropolyfloc area, g is the gravitational acceleration, γ is the fluid dynamic viscosity, r_{eq} is the equivalent radius and v is the velocity.

Van der Waals attractive force $\vec{F}_A$ and electrostatic repulsive force $\vec{F}_R$, were implemented into this PBM to account for the double layer forces, with their modulus being defined as (e.g., Hamaker, 1937; Bhattacharjee et al., 1998)

$$F_A = H_A \frac{r_{eq_i} r_{eq_j}}{6d^2\left(r_{eq_i} + r_{eq_j}\right)}, \tag{5}$$

$$F_R = -\phi^2 \frac{4\pi\varepsilon_0\varepsilon_r\kappa r_{eq_i} r_{eq_j}}{r_{eq_i} + r_{eq_j}} \exp(-\kappa d) \quad (6)$$

where H_A is the Hamaker constant, r_{eq_i} and r_{eq_j} are the equivalent radii of spheropolyflocs i (receiving particle) and j (approaching particle), respectively, d is the distance between the spheropolyflocs surface, $\varepsilon_0 = 8.854 \times 10^{-12}$ F/m is the permittivity of vacuum, $\varepsilon_r = 78.5$ is the dielectric constant of water at 25 °C, $\kappa = 1/0.98$ nm^{-1} is the reciprocal Debye length, and ϕ is the surface electric potential.

Spheropolyfloc surface interactions were determined by vertex to edge contacts. At each contact point, the contact force $\vec{F}_C$ was the resultant of elastic $\vec{F}_E$ and viscous $\vec{F}_V$ forces expressed in their normal and tangential components as $\vec{F}_C = \vec{F}_{En} + \vec{F}_{Et} + \vec{F}_{Vn} + \vec{F}_{Vt}$. The modulus of elastic forces in $\vec{F}_E$ are

$$F_{En} = -k_n \Delta x_n, \quad (7a)$$

$$F_{Et} = -k_t \Delta x_t. \quad (7b)$$

where k_n and k_t are the normal and tangential coefficients of stiffness, which account for the deformation of kaolinite aggregates, Δx_n is the overlapping length between two spheropolyflocs in contact, and Δx_t is the tangential elastic displacement. No sliding condition was assumed. The modulus of viscous forces in $\vec{F}_V$ are defined as

$$F_{Vn} = -M\lambda_n v_n, \quad (8a)$$

$$F_{Vt} = -M\lambda_t v_t. \quad (8b)$$

where λ_n and λ_t are the normal and tangential coefficients of damping, v_n and v_t are the normal and tangential components of contact velocity, respectively, and $M = (m_i m_j)/(m_i + m_j)$ is the effective mass with m_i and m_j the masses of spheropolyflocs i and j, respectively.

A summary of parameters used in Eq. (5) to Eq. (8) is given in Table 1. k_n was estimated as $k_n = YA_p/L$, where A_p is the projected area, L is the spheropolyfloc length perpendicular to that projected area, and Y is the Young's modulus (Alonso-Marroquin et al., 2013). For Y in the order of magnitude of 10^6 N m^{-2} (McFarlane et al., 2005) and the ratio A_p/L, with $L = 2r_{eq}$, changing only slightly for the observed kaolinite aggregates, we obtained $k_n = 20$ N m^{-1}. Values of k_t were derived to satisfy the relationship $k_t/k_n = (1 - 3\nu)/(1 + \nu)$ (Wang and Mora, 2008), with $\nu = 0.28$ being the typical Poisson ratio of clay (Vikash and Prashant, 2008). λ_n was calculated to satisfy critical damping condition, *i.e.*, collision time $t_c = \pi/\sqrt{\omega_0^2 - (\lambda_n/2)^2} \to \infty$, where $\omega_0 = \sqrt{k_n/M}$ is the normal oscillation frequency of the contact between the two spheropolyflocs (Luding, 1998). The limit above implied that $\lambda_n \to 2\omega_0$. Finally, λ_t was calculated using the ratios $\lambda_t/\lambda_n = k_t/k_n$ for the restitution parameters in the normal and tangential directions. Typical values of Hamaker constant H_A and surface electric potential ϕ for kaolinite mineral were from Zhang and Zhang (2011).

Table 1 – Values of parameters used in Eqs. (5)–(8) for each spheropolyfloc collision type (I, II and III). [a]Values of λ_n depended on the effective mass of spheropolyflocs and were calculated as described in Section 2.4.

Parameters	Type I	Type II	Type III
k_n (N m^{-1})	20	20	20
k_t (N m^{-1})	2	2	2
λ_n (s^{-1})	[a]2.1×10^5	[a]7.4×10^5	[a]1.2×10^6
λ_t (s^{-1})	2.1×10^4	7.4×10^4	1.2×10^5
H_A (N m)	1.0×10^{-18}	1.0×10^{-18}	1.0×10^{-18}
ϕ (mV)	15	15	15
r_{eq_i} (μm)	16.41	4.95	4.62
r_{eq_j} (μm)	23.02	23.02	4.95

2.5. *Ortho-axial and peri-axial collisions*

Two different spheropolyflocs i (receiving) and j (approaching) with similar *RE* were used to model ortho-axial (frontal) and peri-axial (tangential) collisions in a gravitational field. Ortho-axial collision was modelled by aligning the spheropolyflocs center of mass, while these were displaced in peri-axial collision by a distance δ ranging from 0 to $\delta_{max} = R_i + R_j$, where R_i and R_j are the distances from the center of mass to the furthest possible contact point.

Experimental r_{eq} were divided into two classes ($r_{eq} \leq 5$ μm and $r_{eq} > 5$ μm, with 5 μm the observed median aggregate size presented later in Section 3.1). Three types of collision were modelled to fully elucidate all possible collision kinetics: Type I, for both r_{eq_i} and r_{eq_j} greater than 5 μm; Type II, for $r_{eq_i} \leq 5$ μm and $r_{eq_j} > 5$ μm; and Type III, for both r_{eq_i} and r_{eq_j} smaller than 5 μm. The orientation of colliding spheropolyflocs in ortho-axial collision were stochastically assigned 1000 times by generating a value n between 0 and 1 with a uniform distribution using *r and* function (in Matlab R2012a), and the angle of orientation θ was determined as $\theta = n2\pi$. Peri-axial collision was modelled using the same orientations of ortho-axial collision, but spheropolyflocs were displaced by various δ values.

The probability of collision and aggregation was then calculated from the set of 1000 stochastic simulations and was analysed for both ortho- and peri-axial collisions and for each of the three collision types (I, II and III).

3. Results

3.1. *Experimental size distribution*

A total of 2596 aggregates were detected in the experimental session, and were used in our analyses. The equivalent radii r_{eq} of these aggregates ranged from 1.69 μm to 35.55 μm, with an average r_{eq} of 6.53 μm and a median at about 5.44 μm (Fig. 2).

3.2. *Optimal spheropolyflocs*

Spheropolyfloc optimization metrics against experimental kaolinite aggregates are depicted in Fig. 3, with the average *RE* in the two size classes $r_{eq} \leq 5$ μm and $r_{eq} > 5$ μm shown as a function of N, and for $r = 1$ μm (panel a), $r = 2$ μm (panel b), and $r = 4$ μm (panel c). The average *RE* of equivalent spheres (*i.e.*,

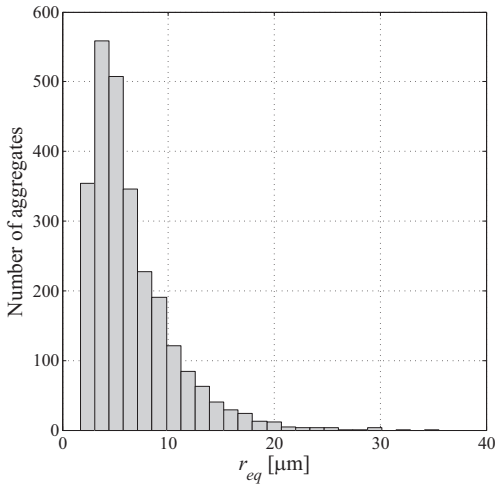

Fig. 2 – Equivalent radius histogram of experimental kaolinite aggregates.

for $N = 1$ and $r = r_{eq}$) was represented in Fig. 3 with dashed lines for comparison.

We note that, all generated spheropolyflocs had substantially smaller *RE* than that of equivalent spheres. We also observe two specific patterns: on the one hand, *RE* increased with increasing *r* in all tests. On the other hand, *RE* of spheropolyflocs with $r_{eq} > 5$ μm decreased with increasing *N* regardless of *r* values tested here. Spheropolyflocs with $r = 1$ μm applied to aggregates with $r_{eq} \leq 5$ μm resulted in a decreasing *RE* with increasing *N* until a minimum was reached at $N = 28$ (Fig. 3a); beyond this point, *RE* seemed to oscillate and presumably reached a steady value. For $r = 2$ μm and $r = 4$ μm (Fig. 3b and c), *RE* was relatively constant over *N* for $r_{eq} \leq 5$ μm.

In agreement with our results, Dobrohotoff et al. (2012) demonstrated that *RE* decreased concordantly with *r*. As the optimization algorithm used binary pixel images, $r = 1$ μm (*i.e.*, equivalent to 1 pixel) was the smallest possible spheroradius. For aggregates with $r_{eq} \leq 4$ μm, spheroradii $r \geq 2$ μm (*i.e.*, about or larger than r_{eq}) tended to result in greater *RE*. Image resolution, therefore, poses a limitation in the use of *r*; it is suggested here that condition $r < r_{eq}$ should be satisfied when using spheropolygons for this purpose.

When condition $r < r_{eq}$ is satisfied, optimization is strictly dependent on the number of vertices *N* in relation to the roundness of a body. As small aggregates have higher degree of roundness, fewer vertices were needed as compared to large aggregates. Hence, assigning a value of *N* greater than the maximum number of vertices in experimental samples tended to produce greater *RE*. This may explain greater *RE* values against an increasing *N* for spheropolyflocs with $r_{eq} \leq 5$ μm (Fig. 3). Alongside, higher image resolution could potentially further decrease *RE*; however, we expect that *RE* would eventually decrease until a minimum point beyond which *RE* would reach a steady value even with increasing *N*, *i.e.*, when the number of vertices is sufficient to describe the actual roundness of a body. Hence, image resolution only limits the use of the spheroradii, while the number of vertices is limited by the actual roundness of a body.

3.3. *Collision probability in the double layer*

The analysis of collision presented here includes both cases of equivalent spheres ($N = 1$ and $r = r_{eq}$) and spheropolyflocs ($N > 1$ and $r > 0$). Each case was investigated for the three collision types (I, II and III).

From a general viewpoint, a collision event *C* between equivalent spheres can result in two events: either $C(d_c < d_0)$, *i.e.*, collision occurs within the attraction zone of the double layer, or $C(d_c \geq d_0)$, *i.e.*, collision occurs outside the attraction zone. Spheres are considered to be within the attraction zone if the distance between centers of mass d_c is smaller than the critical distance d_0 where $\vec{F}_A + \vec{F}_R = 0$, *i.e.*, $d_c < d_0$. In either event $C(d_c < d_0)$ or $C(d_c \geq d_0)$, the collision outcome of spheres will not depend on the external shape but only on the relative size and surface electrochemical characteristics. For the cases analysed here, the size of experimental kaolinite aggregates spanned within a relatively narrow range and only differed by one order of magnitude, and thus, the difference in collision outcome was likely to depend more on electrochemical characteristics than sizes. Our results show that both ortho-axial ($\delta = 0$) and peri-axial ($0 < \delta \leq \delta_{max}$) collisions between

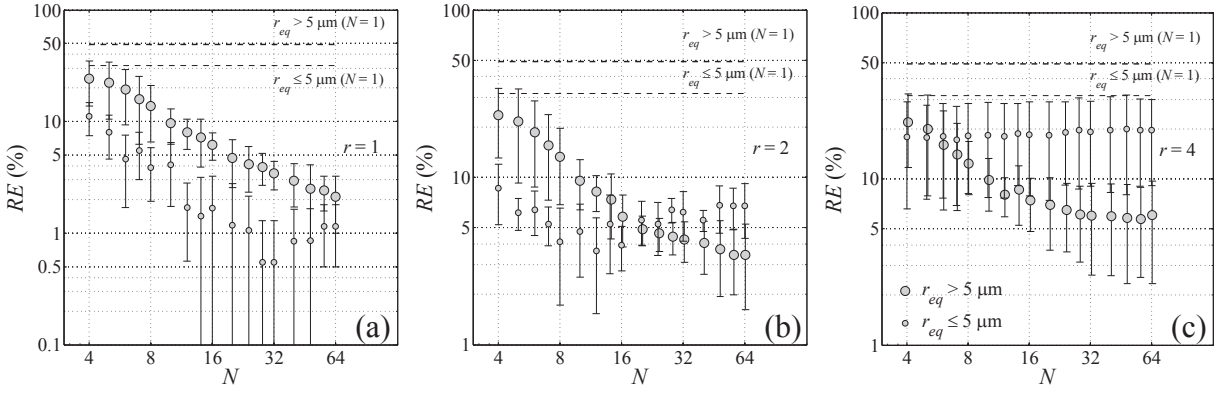

Fig. 3 – Average and standard deviation of the relative error percent RE(%) of generated spheropolyflocs in size classes $r_{eq} \leq 5$ μm (5 samples) and $r_{eq} > 5$ μm (5 samples) as a function of N and for (a) $r = 1$ μm, (b) $r = 2$ μm and (c) $r = 4$ μm, with dashed lines representing the average RE(%) of equivalent spheres (i.e., $N = 1$ and $r = r_{eq}$).

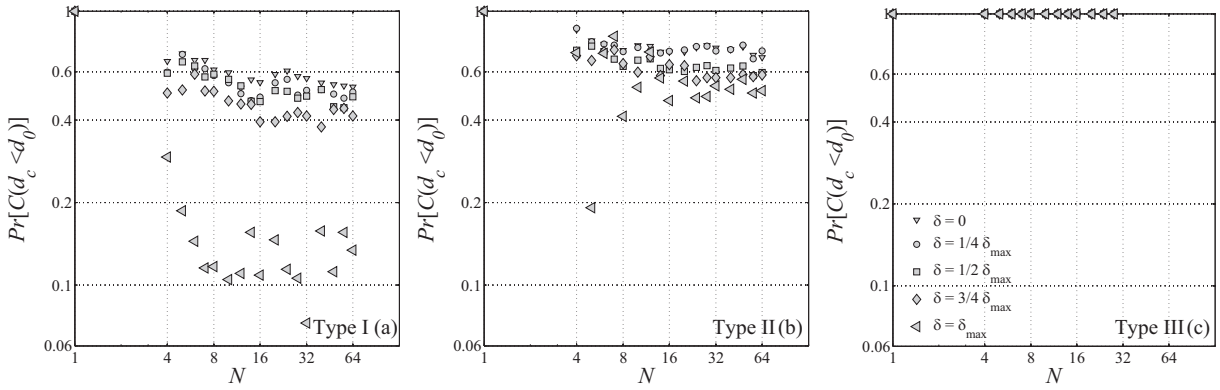

Fig. 4 – Probability of collision within the attraction zone Pr[C(d_c < d_0)] for (a) Type I, (b) Type II, and (c) Type III collisions, with δ ranging from 0 to δ_{max}. The number of vertices N on the *x*-axis refers to that of the approaching spheropolyfloc in each collision type.

spheres of different sizes always resulted in collision within the attraction zone (see Fig. 4 for $N = 1$), and this is regardless of whether the collision was of Type I, II or III.

Collisions between spheropolyflocs were modelled using two spheropolyflocs with spheroradius $r = 1$ μm (tests with $r > 1$ μm were excluded after our analysis in Section 3.2) and similar *RE*. The latter condition did not necessarily imply spheropolyflocs with identical *N*. Conversely to equivalent spheres, collision between spheropolyflocs within or outside the attraction zone is a stochastic event that depends on the surface asperities and relative orientation. To assess the effect of external shape, the probability $Pr[C(d_c < d_0)]$ that collision occurred within the attraction zone of the double layer was calculated for 1000 stochastic replicates in each collision type. Fig. 4 shows that $Pr[C(d_c < d_0)]$ of Type I and II collisions decreased with increasing *N* and also with increasing δ. For Type III collision (between spheropolyflocs with $r_{eq} \leq 5$ μm), the probability $Pr[C(d_c < d_0)] = 1$ for all *N* and δ values. This complies with the fact that d_0 was of similar order of magnitude as the size of aggregates. Among the three collision types, Type I generally showed the lowest $Pr[C(d_c < d_0)]$, and was followed by Type II and III. The collision interaction between aggregates with $r_{eq} > 5$ μm also showed the highest sensitivity to δ. This may be due to large aggregates ($r_{eq} > 5$ μm) having greater surface peculiarities than small aggregates ($r_{eq} \leq 5$ μm), thus leading to shape effects on collision location more evident than in other collision types.

These results give an evidence that the outer shape of aggregates may play an important role in determining whether a collision would occur within or outside the double layer field. Note, however, that this information is not enough to determine *a priori* if a collision within the attraction zone would have aggregation as an outcome.

3.4. *Aggregation probability*

If one presumes that aggregation were only be governed by the van der Waals attractive force $\vec{F}_A$, all collisions occurring within the attraction zone should lead to aggregation in opposition to those occurring outside; mathematically, this could be written as $Pr[A|C(d_c < d_0)] = 1$, where $A|C(d_c < d_0)$ is an event of aggregation when a collision occurred in the attraction zone. However, as anticipated earlier, collision within the attraction zone is neither necessary a condition nor it is sufficient for aggregation to happen in that zone. In fact, external shape is the factor that determines an outcome, and this

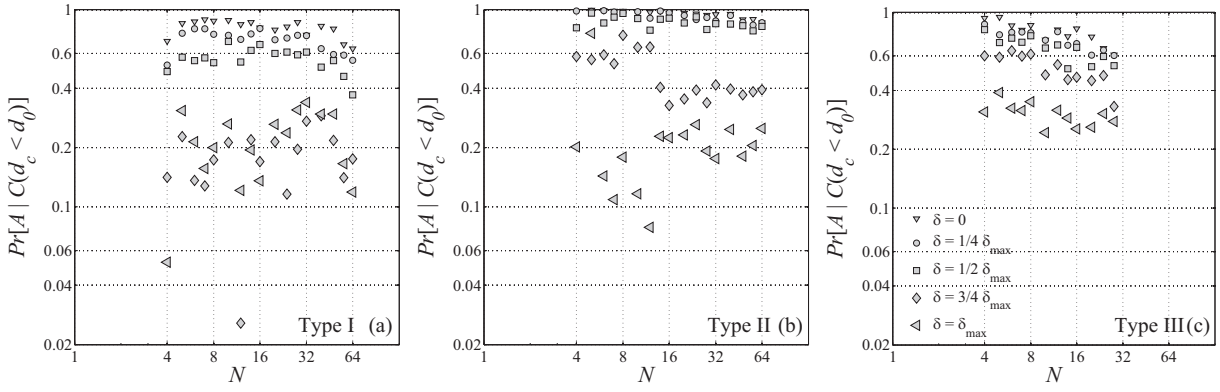

Fig. 5 – Conditional probability of aggregation after collision occurring within the attraction zone $Pr[A|C(d_c < d_0)]$ for (a) Type I, (b) Type II, and (c) Type III collisions, with δ ranging from 0 to δ_{max}. The number of vertices N on the *x*-axis refers to that of the approaching spheropolyfloc in each collision type.

factor is discussed in detail here for equivalent spheres and spheropolyflocs.

For the tests using equivalent spheres, the outcome of collision was found to always result in aggregation ($Pr[A] = 1$) because spheres did not have surface peculiarities. The relative rotation over one another would never bring their centers of mass beyond d_0 and, hence, $\overrightarrow{F}_A > \overrightarrow{F}_R$ would hold regardless of δ and collision type (Fig. 5).

When spheropolyflocs collided and rotated over the surface of each other, surface asperities could move their centers of mass into or beyond d_0. Results in Fig. 5 show that the aggregation probability after collision occurring within the attraction zone was $Pr[A|C(d_c < d_0)] < 1$ in all cases. Generally, $Pr[A|C(d_c < d_0)]$ decreased with increasing N and increasing δ for the three collision types. Type II collision showed the highest $Pr[A|C(d_c < d_0)]$, while Type I and III collisions had lower probability. Note that although Type I and III involved spheropolyflocs of different size classes, these had very similar aggregate size ratios r_{eq_j}/r_{eq_i} and, hence, were expected to have similar probability of aggregation (e.g., *Overbeek, 1952*; *Hogg* et al., 1966).

On the other hand, the aggregation probability after collision occurring outside the attraction zone was $Pr[A|C(d_c \geq d_0)] > 0$ in Type I and II collisions (Fig. 6). These probabilities $Pr[A|C(d_c \geq d_0)]$ decreased with increasing N and increasing δ. In Type I collision, $Pr[A|C(d_c \geq d_0)]$ always equalled 0 when $\delta = \delta_{max}$. We also observed that in general, $Pr[A|C(d_c \geq d_0)] < Pr[A|C(d_c < d_0)]$ in all cases, and that both Type I and II collisions had relatively similar $Pr[A|C(d_c \geq d_0)]$. The probability $Pr[A|C(d_c \geq d_0)]$ in Type III collision was not shown because collisions always occurred inside the attraction zone as depicted in Fig. 4c. These results demonstrate the importance of external shape, not only in determining the location of collision in the double layer, but also in conditioning whether a collision would result in aggregation.

3.5. *Relative trajectory of spheropolyflocs*

With the capability to track the relative position of interacting spheropolyflocs, we could analyse their trajectory before and after collision.

We identified four types of trajectory, each representing one possible interaction mechanism: Trajectory A (Fig. 7a) describes two spheropolyflocs colliding within d_0 and rotating over the surface of each other with their centers of mass always inside the attraction zone and, thus, resulting in aggregation; Trajectory B (Fig. 7b) represents a collision within the attraction zone with the centers of mass of spheropolyflocs falling beyond d_0 during rotation, thus, causing them to repel and depart from each other; Trajectory C (Fig. 7c) shows a collision occurring beyond d_0 that results in aggregation after relative rotation moves their centers of mass into the attraction zone; and finally, Trajectory D (Fig. 7d) describes the case where a collision occurs outside the attraction zone and does not lead to aggregation.

Interaction mechanisms between spheropolyflocs in each of the three collision types were investigated. The probability of the four types of trajectory was calculated from 5000 stochastic replicates with δ ranging from 0 to δ_{max} (Fig. 8). Here, we observed very distinct patterns in the occurrence of different relative trajectories among the three collision types. Trajectory D was observed in approximately 50% of Type I collisions, and the probability increased with increasing N. In Type II collision, Trajectory A was observed to be the most frequent interaction mechanism but the occurrence of this trajectory decreased as N increased. On the other hand, only Trajectory A and B were observed in Type III collision, with the probability of Trajectory A decreasing with increasing N.

These results suggest that the relative size of colliding spheropolyflocs influences the way and mechanisms by which they interacted, and implies that the effect of external shape observed in one collision type may not be directly applicable to collision of another type.

4. Discussion

We have highlighted several aspects of collision dynamics of irregularly-shaped kaolinite aggregates, but we also recall that there are several additional aspects that need to be discussed.

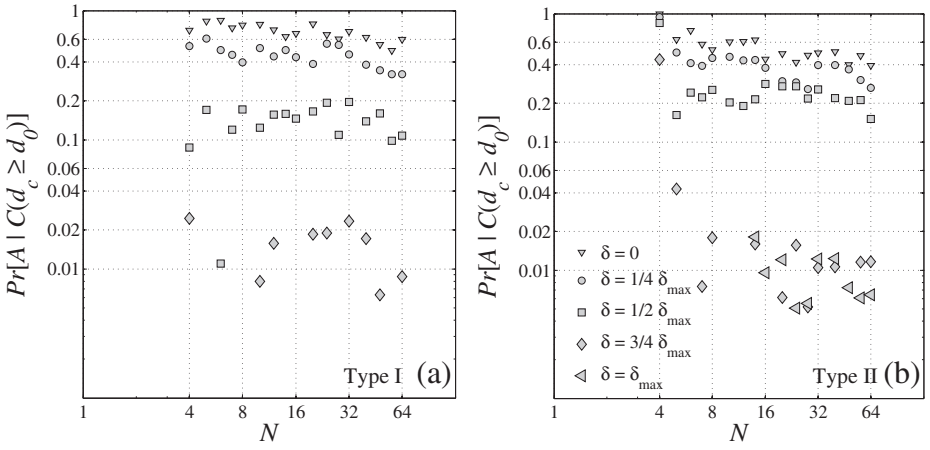

Fig. 6 – Conditional probability of aggregation after collision occurring outside the attraction zone $Pr[A|C(d_c \geq d_0)]$ for (a) Type I, and (b) Type II collisions, with δ ranging from 0 to δ_{max}. The number of vertices N on the x-axis refers to that of the approaching spheropolyfloc in each collision type.

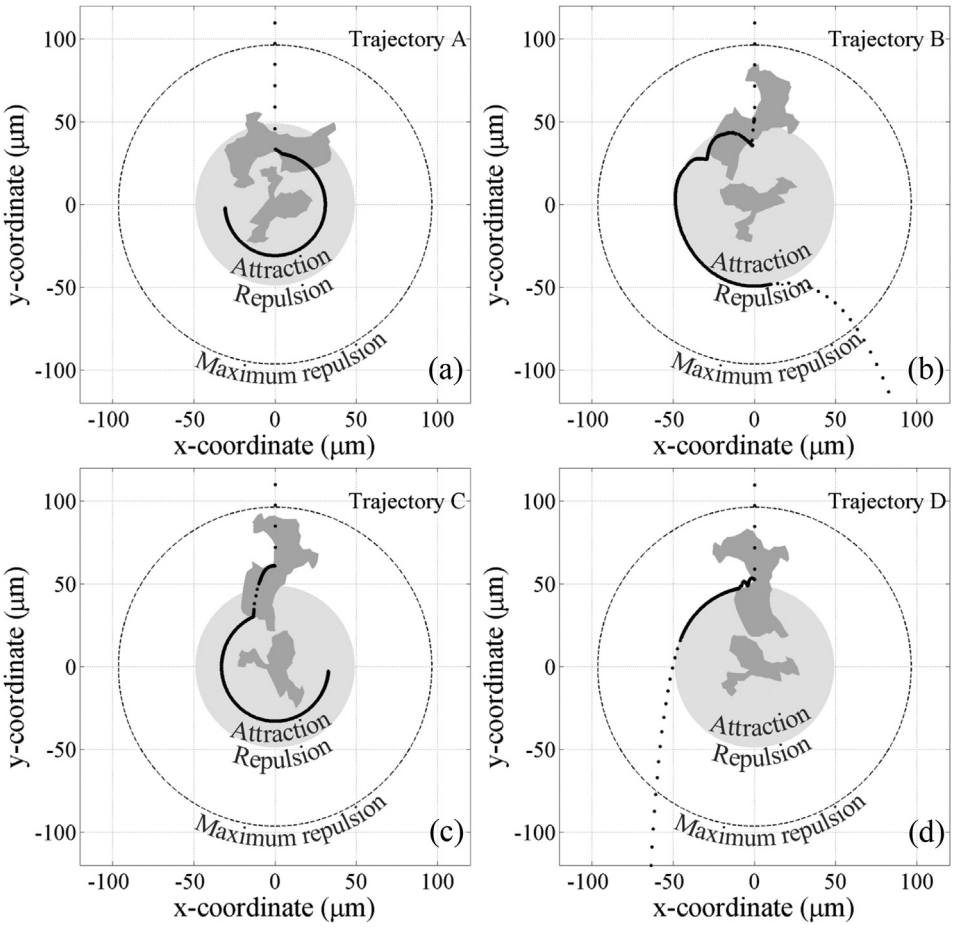

Fig. 7 – Trajectories of spheropolyflocs with $N = 64$ and $r = 1$ μm in Type I ortho-axial collision ($\delta = 0$) for the cases where the collision occurred (a) within d_0 and resulted in aggregation (Trajectory A), (b) within d_0 and did not lead to aggregation (Trajectory B), (c) beyond d_0 and led to aggregation (Trajectory C) and (d) beyond d_0 with no aggregation observed (Trajectory D).

The internal aggregate architecture, porosity and fractal dimension are presumably affecting collision interaction and aggregation probability, whereas the aggregates in this PBM were considered as solid bodies. Some previous studies suggest that collisions between porous and fractal aggregates resulted in a higher aggregation probability as compared to that of rigid, non-porous spheres (e.g., Serra and Logan, 1999; Kim and Stolzenbach, 2004). Pores would increase the capture efficiency of particles and aggregates, and hence the probability of aggregation, presumably due to flow through internal open pores (e.g., Li and Logan, 1997; Kim and Stolzenbach, 2004). Higashitani et al. (2001) suggested that deformation of the internal structure of aggregates, which led to aggregate breakup, is important for porous aggregates, especially when water flows through the pores. However, in this manuscript, we assumed that the effect of collision-induced deformation has a second order relevance on the collision outcome, while we recognized this aspect to possibly cause nonlinearities that may require further investigation. Note that pores could be included in the approach presented here using aggregate made of several spheropolyflocs solidly attached to their neighbours. The case was not presented here yet as it was beyond the purpose of this manuscript; however, research in this direction is expected to elucidate interaction mechanisms to further detail.

Our analysis was limited to binary collisions between equivalent spheres and spheropolyflocs, and hence, we have excluded the possible effects of simultaneous collision of multiple aggregates. We do believe, though, that the time scales of binary collision can be considered much smaller than the time lap needed between two sequential collisions to occur. Multiple collision can therefore be dealt with as a sequence of binary collision, provided that the integration time step is small enough (smaller than the average collision time lapse).

Hydrodynamics is the driving force of most processes and mechanisms in natural water bodies and, hence, the interaction between fluid and particles dynamics could be important. Flocculation, and aggregation and breakup rates are known to be highly affected by the turbulence shear rate (e.g., Winterwerp, 1998; Maggi, 2005). Some earlier studies have suggested that by taking into consideration wake effects, the presence of a large particle may cause an increase in the settling velocity of small particle and may tend to cause small particle to elude from capture (e.g., McCave, 1984; Han and Lawler, 1991; Zhu et al., 1994). However, fluid motion was not described in our model and, therefore, the effects of wake and

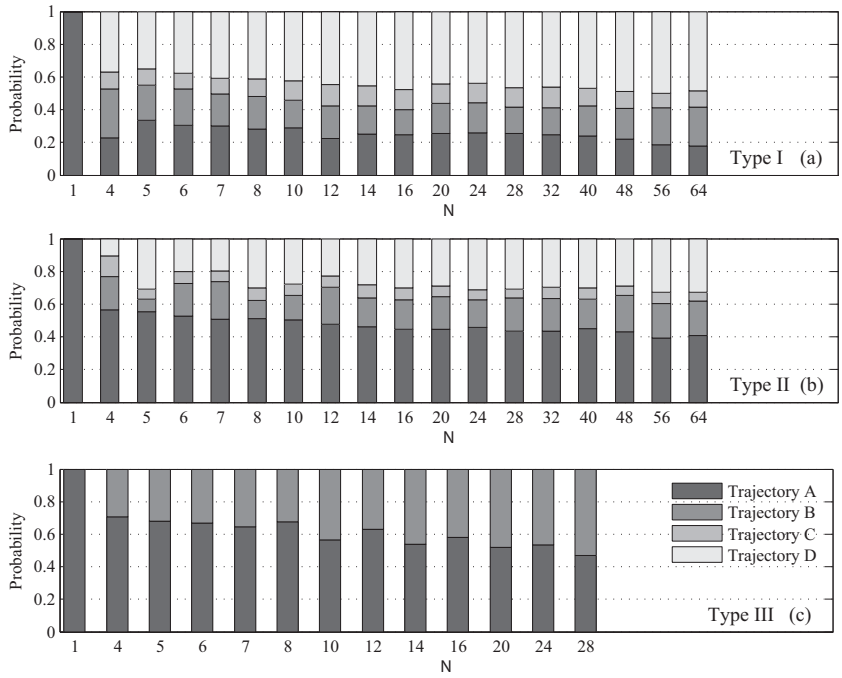

Fig. 8 – Probability of four different types of trajectory (A, B, C and D) in 5000 stochastic replicates with δ ranging from 0 to δ_{max} for (a) Type I, (b) Type II, and (c) Type III collisions. The number of vertices N on the x-axis refers to that of the approaching spheropolyfloc in each collision type.

hydrodynamics on the aggregation dynamics of SPM were not included explicitly. Although these may be important aspects to be elucidated with this model, results in Sections 3.3 and 3.4 highlighted the role of the outer aggregate shape on the probability of aggregation, that is the main focus of this work.

The drag force acting on a particle would potentially be affected by its shape. In this manuscript, we adopted a simplified assumption, that is, replacing the complex shape by an equivalent sphere in the calculation of Stokes' velocity. Although considering the shape of aggregates within Navier–Stokes equations would improve the estimation of settling velocity, the collision dynamics would not be significantly affected. Taking into account the shape within the Navier–Stokes framework would be beneficial in sediment dynamics modelling where the Stokes' settling velocity would require to be superseded by a more accurate expression.

Overall, the morphological analyses in this work have highlighted the capability of spheropolygon theory to capture the details of aggregate external shape and the extent to which it can affect collision and aggregation in a two-dimensional binary system.

5. Conclusion

This study puts forward an approach to approximate the external shape of kaolinite aggregates using the spheropolygon theory and highlights the effects of shape in collision and aggregation dynamics. The major findings of this study can be summarized as follows: (i) spheropolyflocs generated based on experimental kaolinite aggregates achieved an error <1% as compared to equivalent spheres with error >32%; (ii) the accuracy of shape description generally increased with increasing number of vertices N and decreasing spheroradius r used in spheropolygon optimization, provided that the condition $r < r_{eq}$ was met; (iii) in all collision cases, equivalent spheres always collided within the attraction zone of the double layer and resulted in aggregation; (iv) in collisions between spheropolyflocs, the probability of collision within the attraction zone $Pr[C(d_c < d_0)]$ and the probability of aggregation $Pr[A]$ generally decreased with increasing N; (v) both $Pr[C(d_c < d_0)]$ and $Pr[A]$ also decreased with increasing displacement between the centers of mass of the two colliding spheropolyflocs, *i.e.*, in the case of peri-axial collisions. We, therefore, conclude that the kinetics of SPM are highly influenced by the surface asperities of aggregates, which can effectively be accounted for by using spheropolygons in mathematical models.

Acknowledgements

The authors thank Mr. Ross Barker and Mr. Theo Gresley-Daines for technical support and assistance, and two anonymous reviewers for their comments on the original manuscript. Fiona Tang was partly supported by the Summer Scholarship Research Program of the School of Civil Engineering, The University of Sydney for this project.

REFERENCES

Abrahamson, J., 1975. Collision rates of small particles in a vigorously turbulent fluid. Chem. Eng. Sci. 30 (11), 1371–1379.

Allen, M.P., Tildesley, D.J. (Eds.), 1993. Computer Simulation in Chemical Physics: proceedings of the Nato Advanced Study Institute on New Perspectives in Computer Simulation in Chemical Physics, vol. 397. Springer, Alghero, Sardinia, Italy.
Alonso-Marroquin, F., 2008. Spheropolygons: a new method to simulate conservative and dissipative interactions between 2D complex-shaped rigid bodies. EPL Europhys. Lett. 83 (1), 14001.
Alonso-Marroqun, F., Ramrez-Gmez, A., Gonzlez-Montellano, C., Balaam, N., Hanaor, D.A., Flores-Johnson, E.A., Shen, L., 2013. Experimental and numerical determination of mechanical properties of polygonal wood particles and their flow analysis in silos. Granul. Matter 15 (6), 811–826.
Anderson, R.F., 1982. Concentration, vertical flux, and remineralization of particulate uranium in seawater. Geochim. Cosmochim. Acta 46 (7), 1293–1299.
Bhattacharjee, S., Elimelech, M., Borkovec, M., 1998. DLVO interaction between colloidal particles: beyond Derjaguin's approximation. Croat. Chem. Acta 71 (4), 883–903.
Boetius, A., Springer, B., Petry, C., 2000. Microbial activity and particulate matter in the benthic nepheloid layer (BNL) of the deep Arabian Sea. Deep-Sea Res. II 47 (14), 2687–2706.
Briggs, L.I., McCulloch, D.S., Moser, F., 1962. The hydraulic shape of sand particles. J. Sediment. Research 32, 645–656.
Clift, R., Grace, J.R., Weber, M.E., 1978. "Bubbles" Drops and Particles. Academic, New York, p. 1870.
Cloern, J.E., 2001. Our evolving conceptual model of the coastal eutrophication problem. Mar. Ecol. Prog. Ser. 210, 223–253.
Corey, A.T., 1949. Influence of Shape on the Fall Velocity of Sand Grains. MS thesis. Colo A and M College, Fort Collins, Colo.
Dietrich, W.E., 1982. Settling velocity of natural particles. Water Resour. Res. 18 (6), 1615–1626.
Dobrohotoff, P.B., Azeezullah, S.I., Maggi, F., Alonso-Marroquin, F., 2012. Optimal description of two-dimensional complex-shaped objects using spheropolygons. Granul. Matter 14 (5), 651–658.
Fowler, S.W., Knauer, G.A., 1986. Role of large particles in the transport of elements and organic compounds through the oceanic water column. Prog. Oceanogr. 16 (3), 147–194.
Gibbs, R.J., Konwar, L.N., 1982. Effect of pipetting on mineral flocs. Environ. Sci. Technol. 16 (2), 119–121.
Hamaker, H.C., 1937. The London-van der Waals attraction between spherical particles. Physica 4 (10), 1058–1072.
Han, M., Lawler, D.F., 1991. Interactions of two settling spheres: settling rates and collision efficiency. J. Hydraul. Eng. 117, 1269–1289.
Herbert, R.A., 1999. Nitrogen cycling in coastal marine ecosystems. FEMS Microbiol. Rev. 23 (5), 563–590.
Higashitani, K., Iimura, K., Sanda, H., 2001. Simulation of deformation and breakup of large aggregates in flows of viscous fluids. Chem. Eng. Sci. 56 (9), 2927–2938.
Hogg, R., Healy, T.W., Fuerstenau, D.W., 1966. Mutual coagulation of colloidal dispersions. Trans. Faraday Soc. 62, 1638–1651.
Janke, N.C., 1966. Effect of shape upon the settling velocity of regular convex geometric particles. J. Sediment. Research 36, 370–376.
Kim, A.S., Stolzenbach, K.D., 2004. Aggregate formation and collision efficiency in differential settling. J. Colloid Interface Sci. 271, 110–119.
Kiorboe, T., 2003. Marine snow microbial communities: scaling of abundances with aggregate size. Aquat. Microb. Ecol. 33 (1), 67–75.
Knowles, R., 1982. Denitrification. In: Microbiological Review, pp. 43–70.
Kranenburg, C., 1994. The fractal structure of cohesive sediment aggregates. Estuar. Coast. Shelf Sci. 39 (6), 451–460.
Krishnappan, B.G., 1990. Modelling of settling and flocculation of fine sediments in still water. Can. J. Civ. Eng. 17 (5), 763–770.
Krone, R.B., 1962. Flume Studies of the Transport of Sediment in Estuarial Shoaling Processes. Final Report. Hydraulic Engineering Laboratory and Sanitary Engineering Research Lab, University of California, Berkerly, California.
Kusters, K.A., Wijers, J.G., Thoenes, D., 1997. Aggregation kinetics of small particles in agitated vessels. Chem. Eng. Sci. 52 (1), 107–121.
Lartiges, B.S., Deneux-Mustin, S., Villemin, G., Mustin, C., Barres, O., Chamerois, M., Gerard, B., Babut, M., 2001. Composition, structure and size distribution of suspended particulates from the Rhine River. Water Res. 35 (3), 808–816.
Laverman, A.M., van Cappellen, P., van Rotterdom-Los, D., Pallud, C., Abell, J., 2006. Potential rates and pathways of microbial nitrate reduction in coastal sediments. FEMS Microbiol. Ecol. 58 (2), 179–192.
Leppard, G.G., Flannigan, D.T., Mavrocordatos, D., Marvin, C.H., Bryant, D.W., McCarry, B.E., 1998. Binding of polycyclic aromatic hydrocarbons by size classes of particulate in Hamilton Harbor water. Environ. Sci. Technol. 32 (22), 3633–3639.
Li, X., Logan, B.E., 1997. Collision frequencies between fractal aggregates and small particles in a turbulently sheared fluid. Environ. Sci. Technol. 31 (4), 1237–1242.
Lick, W., Rapaka, V., 1996. A quantitative analysis of the dynamics of the sorption of hydrophobic organic chemicals to suspended sediments. Environ. Toxicol. Chem. 15 (7), 1038–1048.
Luding, S., 1998. Collisions and contacts between two particles. In: NATO ASI Series E Applied Sciences-Advanced Study Institute, vol. 350, pp. 285–304.
Maggi, F., 2005. Flocculation Dynamics of Cohesive Sediments. Ph.D. Thesis. Delft Universitiy of Technology, The Netherlands.
Maggi, F., 2007. Variable fractal dimension: a major control for floc structure and flocculation kinematics of suspended cohesive sediment. J. Geophys. Res. 112, C07012. http://dx.doi.org/10.1029/2006JC003951.
Maggi, F., 2009. Biological flocculation of suspended particles in nutrient-rich aqueous ecosystems. J. Hydrol. 376, 116125.
Maggi, F., 2013. The settling velocity of mineral, biomineral and biological particles and aggregates in water. J. Geophys. Res. Oceans 118 (4), 2118–2132.
McCave, I.N., 1984. Size spectra and aggregation of suspended particles in the deep ocean. Deep Sea Res. Part Oceanogr. Res. Pap. 31 (4), 329–352.
McFarlane, A.J., Addai-Mensah, J., Bremmell, K., 2005. Rheology of flocculated kaolinite dispersions. Korea-Aust. Rheol. J. 17 (4), 181–190.
Meakin, P., 1991. Fractals aggregates in geophysics. Rev. Geophys. 29.
Ongley, E.D., Bynoe, M.C., Percival, J.B., 1981. Physical and geochemical characteristics of suspended solids, Wilton Creek, Ontario. Can. J. Earth Sci. 18 (8), 1365–1379.
Overbeek, J.Th.G., 1952. Electorchemistry of the double layer. Colloid Sci. 1, 115–193.
Riebesell, U., 1991. Particle aggregation during a diatom bloom: 2 biological aspects. Mar. Ecol. - Prog. Ser. 69 (3), 281–291.
Rubey, W.W., 1933. Settling velocity of gravel, sand, and silt particles. Am. J. Sci. 148, 325–338.
Saffman, P., Turner, J.S., 1956. On the collision of drops in turbulent clouds. J. Fluid Mech. 1 (16), 16–30.
Serra, T., Casamitjana, X., 1998. Structure of the aggregates during the process of aggregation and breakup under a shear flow. J. colloid interface Sci. 206 (2), 505–511.
Serra, T., Logan, B.E., 1999. Collision frequencies of fractal bacterial aggregates with small particles in a sheared fluid. Environ. Sci. Technol. 33 (13), 2247–2251.
Simon, M., Grossart, H.P., Schweitzer, B., Ploug, H., 2002. Microbial ecology of organic aggregates in aquatic ecosystems. Aquat. Microb. Ecol. 28, 175–211.

Stokes, G.G., 1851. On the Effect of the Internal Friction of Fluids on the Motion of Pendulums, vol. 9. Pitt Press.
Stolzenbach, K.D., 1993. Scavenging of small particles by fast-sinking porous aggregates. Deep Sea Res. 40 (2), 359–369.
Stone, M., Krishnappan, B.G., 2003. Floc morphology and size distributions of cohesive sediment in steady-state flow. Water Res. 37 (11), 2739–2747.
Tye, R., Jepsen, R., Lick, W., 1996. Effects of colloids, flocculation, particle size and organic matter on the adsorption of hexachlorobenzene to sediments. Environ. Toxicol. Chem. 15 (5), 643–651.
Vahedi, A., Gorczyca, B., 2011. Application of fractal dimensions to study the structure of flocs formed in lime softening process. Water Res. 45 (2), 545–556.
Vainshtein, P., Shapiro, M., Gutfinger, C., 2004. Mobility of permeable aggregates: effects of shape and porosity. Aerosol Sci. 35, 383–404.
Valioulis, I.A., List, E.J., 1984. Collision efficiencies of diffusing spherical particles: hydrodynamic, van der Waals and electrostatic forces. Adv. Colloid Interface Sci. 20 (1), 1–20.
van Leussen, W., 1999. The variability of settling velocities of suspended fine-grained sediment in the Ems estuary. J. Sea Res. 41 (1), 109–118.
Vikash, G., Prashant, A., 2008. Issues in modeling the stress-strain behavior of Kaolin Clay with dispersed microfabric. In: The 12th International Conference of IACMAG.
Wacholder, E., Sather, N.F., 1974. The hydrodynamic interaction of two unequal spheres moving under gravity through quiescent viscous fluid. J. Fluid Mech. 65 (3), 417–437.
Wang, Y., Mora, P., 2008. Macroscopic elastic properties of regular lattices. J. Mech. Phys. Solids 56, 3459–3474.
Winterwerp, J.C., 1998. A simple method for turbulence induced flocculation of cohesive sediment. J. Hydraul. Res. 36 (3), 309–326.
Winterwerp, J.C., 1999. On the flocculation and settling velocity of estuarine mud. Cont. Shelf Res. 22 (9), 1339–1360.
Wu, R.M., Lee, D.J., 2001. Hydrodynamic drag on non-spherical floc and free-settling test. Water Res. 35 (13), 3226–3234.
Zhang, J.F., Zhang, Q.H., 2011. Lattice Boltzmann simulation of the flocculation process of cohesive sediment due to differential settling. Cont. Shelf Res. 31 (10), s94–s105.
Zhu, C., Liang, S.C., Fan, L.S., 1994. Particle wake effects on the drag force of an interactive particle. Int. J. Multiph. Flow. 20 (1), 117–129.